Final form published in Materials Research Bulletin. https://doi.org/10.1016/j.materresbull.2022.111844

Structural, optical and electrical properties of evaporated kesterite films with different off-stoichiometric type

P. Martínez-Ortiz[1], J. F. Trigo[1], N. Pineda-Aguilar[2], C. Guillén[1,*]

[1]Centro de Investigaciones Energéticas, Medioambientales y Tecnológicas (CIEMAT) Avda. Complutense 40, 28040-Madrid, Spain. *Corresponding author, c.guillen@ciemat.es

[2]Centro de Investigación en Materiales Avanzados, S.C. (CIMAV), Subsede Monterrey, Parque de Investigación e Innovación Tecnológica, 66628-Apodaca, Nuevo León, Mexico.

Abstract:

Kesterite thin films with four different off-stoichiometry have been synthetized by sequential evaporation of ternary (Cu_2SnS_3 or Cu_3SnS_4) and binary (ZnS) layers, following sulfurization (with elemental S) at 450 ºC or 500 ºC. Zn-poor compositions (Zn/Sn < 1.0) are used to study the effect of substitutional Sn_{Zn} defects, together with V_{Zn} defects when Cu/Sn ~ 2.0 (sample CZTS1) or with Cu_{Zn} defects for Cu/Sn > 2.0 (sample CZTS2). Besides, the effect of cationic disorder is also studied for Zn/Sn ~ 1.0, producing Zn_{Cu} and Sn_{Cu} defects when Cu/Sn ~ 2.0 (sample CZTS3) or Cu_{Zn} and Cu_{Sn} for Cu/Sn > 2.0 (sample CZTS4). The crystalline structure, morphology, optical and electrical properties of the different samples have been analyzed comparatively by X-ray diffraction (XRD), scanning electron microscopy (SEM), spectrophotometry and coplanar electrical measurements. The highest crystallinity was achieved by the reaction of Cu_3SnS_4 and ZnS (sample CZTS4) at 450 ºC, with a wide bandgap and low resistivity, which remain unchanged when increasing the heating temperature to 500 ºC.

Keywords: Chalcogenides; thin films; evaporation; electronic properties, optical properties.

1. Introduction

Cu_2ZnSnS_4 (CZTS) belongs to the kesterite family, isoelectronic equivalent of the chalcopyrite $Cu(In,Ga)S_2$, replacing scarce elements (In and Ga) with more abundant ones (Zn and Sn), which makes it a good candidate for the next generation of cheap and environment-friendly optoelectronic devices. The kesterite compound exhibits a high optical

absorption and p-type conductivity, like its chalcopyrite analog, demonstrating good performance in thin film photovoltaics, photodetectors, gas sensors, energy storage, and many more [1].

The major barrier limiting the kesterite performance is related to the control of structural defects [2], which are emphasized due to the great flexibility of the quaternary compound. The structural flexibility is due to the predisposition of kesterite to stabilize different defects (vacancies, interstitials and anti-sites) ensuring charge balance through suitable substitutions at cationic positions. According to theoretical calculations, the kesterite structure is prone to defects related to cationic disorder, such as Cu_{Zn}, Cu_{Sn}, Zn_{Cu}, Zn_{Sn}, Sn_{Cu}, and Sn_{Zn}, which associate to form thermodynamically stable clusters [3]. The antisite defect cluster $Cu_{Zn}+Zn_{Cu}$ shows the lowest formation energy, indicating that a large number of these clusters may exist in the kesterite lattice with near-stoichiometric composition [4], leading to a decrease in the bandgap [3].

Moreover, the interrelationship between off-stoichiometry and lattice defects is critical to the understanding and development of kesterite-based devices. Several investigations on powder materials have demonstrated the ability of the CZTS compound to admit changes in composition, maintaining the kesterite structure with atomic proportions of Zn/Sn and Cu/(Zn+Sn) higher or lower than unity [5–7]. Single-phase kesterite structure was found in powder materials within the composition limits $0.5 \leq Zn/Sn \leq 1.6$ and $0.6 \leq Cu/(Zn+Sn) \leq 1.7$, while off-stoichiometric kesterite coexisting with secondary phases were found outside of these ranges [7].

Assuming that cations and anions maintain their respective oxidation states in kesterites with different atomic ratios, only some particular substitutions can achieve the charge balance, allowing each off-stoichiometric composition to be related to a certain defect cluster. This interrelation is established in the ‘off-stoichiometry model’, which summarizes twelve kesterite types (denoted as type A-L) according to the specific Cu/(Zn+Sn) and Zn/Sn ratios and the corresponding defect complex [6,8]. The full model is supported by polycrystalline powder samples [5–7], while only a few off-stoichiometry types have been studied in thin film form [9–11]. In these cases, the number of point defects and defect clusters depends on the film deposition conditions [10,11], and the presence of metastable states is attributed to poor relaxation of defects during the cool-down process [9]. Postdeposition annealing treatments with slow cooling rates can effectively remove secondary phases and metastable states, improving the ordering degree and the bandgap of kesterite thin films [12,13].

In the present work, kesterite CZTS thin films with different off-stoichiometry have been synthetized by sulfurization of sequentially evaporated ternary (Cu_2SnS_3 or Cu_3SnS_4, both denoted as CTS) and binary (ZnS) layers, following the deposition conditions that were optimized previously [14]. The chosen procedure allows to obtain CZTS samples with controlled composition, avoiding the loss of Sn (which is harder from ternary CTS than from binary SnS [15]), and setting the stoichiometry along a Cu-rich line (Cu/Sn $\geq$ 2.0) that benefits cation arrangement [16]. Besides, the Zn ratio is chosen low (Zn/Sn $\leq$ 1.0) to minimize the well-known Zn_{Cu} defects, favoring instead the formation of other point defects like Sn_{Zn} or V_{Zn}, which are less investigated in kesterite thin films. In this way, four kesterite types with few experimental data have been chosen to study. The objective is to analyze comparatively these different types to determine the best route for achieving kesterite films with improved structural, optical and electrical characteristics.

2. Experimental procedure

CZTS formation was achieved by sulfurization of CTS and ZnS films evaporated on soda-lime glass substrates. **The evaporation chamber contains Knudsen cells for metals and a valved cracker effusion cell for sulfur, using infrared lamps to heat the substrates**. **Quartz sensors were used to monitor the evaporation rate of each component and adjust the source temperature accordingly during the process**. First, a CTS film was grown at 350 ºC with 0.20 μm thickness and different atomic ratios that correspond to **cubic** Cu_2SnS_3 (with Cu/Sn = 2.0 or 2.3) and **orthorhombic** Cu_3SnS_4 (with Cu/Sn = 3.0), **as shown in Figure S1 of the supplementary information file,** which is according to the results obtained in previous works [17,18]. Subsequently, a ZnS film with 0.05 or 0.10 μm thickness was evaporated on the CTS layer kept at 200 ºC, resulting in two different Zn to Sn ratios (Zn/Sn = 0.5 or 1.0). Table 1 shows a summary of the precursors chosen and the corresponding target composition for each sample. Finally, the CTS and ZnS stacked layers were sulfurized **in a tubular furnace with infrared lamps around the outside of the tube** (with elemental S placed near to the sample) at 450 ºC or 500 ºC during 1 h to complete the CZTS formation. A slow rate (10 ºC/min) has been chosen for heating and cooling to enhance the reaction homogeneity and minimize metastable defects.

The morphology and elemental composition of the samples heated at 450 ºC or 500 ºC were examined by a field emission scanning electron microscope (FESEM) (Nova NanoSEM 200, FEI Company), which was equipped with an energy-dispersive X-ray analyzer (INCA X-Sight EDS detector, Oxford Instruments). The crystallographic properties were analyzed by

X-ray diffraction (X'Pert instrument, PANalytical) using the nickel-filtered Kα1 emission line of copper (λ = 1.5405 Å), **with a monochromator**, in Bragg-Brentano (θ − 2θ) configuration. **The angular step size was 0.02 º and the acquisition time 2 seconds per step.** The recorded diffraction peaks were compared to the standard **powder diffraction files (PDF)**.

Electrical measurements were performed with a programmable voltage source and current electrometer (Keithley 2420), placing four electric contacts (two for sweep V and two to measure I) in coplanar configuration on the sample. Resistance and resistivity are connected by the relation R = ρ (F/t) [19], where R is the electric resistance obtained from the I-V slope, ρ the electrical resistivity, t the film thickness, and F a geometrical factor that is 0.23 for the configuration used. Optical transmittance (T) and reflectance (R) measurements were carried out in a double beam spectrophotometer (Perkin-Elmer Lambda 9) with unpolarized light from 300 to 1800 nm in wavelength. The fraction of light absorbed, A(%) = 100 – T(%) – R(%), is obtained as a function of the light energy for each sample and the bandgap energy is calculated by the inflection point method [20,21]. **Photoluminescence measurements were made in a fluorescence spectrophotometer (Cary Eclipse) using a xenon lamp with a monochromator set at a wavelength of 787 nm as excitation source, while the emission was recorded in a spectral range from 800 to 950 nm.**

3. Results and discussion

The atomic percentages (at. %) determined by EDX analysis for the various CZTS thin films are summarized in Table 2. These data show a good agreement with the targeted composition (in Table 1) for both heating temperatures (450 ºC and 500 ºC), which discards the loss of volatile elements or compounds during the annealing. According to previous studies [15], the different phases have evaporation rates that increase in the way Cu_2ZnSnS_4 < Cu_4SnS_4 < Cu_2SnS_3 < SnS, with an important loss of SnS from the CZTS films at temperatures ≥ 550 ºC [22,23]. Here, such temperature limit was not exceeded in order to maintain good control of stoichiometry after heating, as has been verified experimentally. Table 2 also includes the kesterite type and the corresponding defects cluster that are assigned for each atomic composition according to the literature [6,8]. Substitutional Sn_{Zn} defects are expected for both Zn-poor compositions (Zn/Sn < 1.0), together with V_{Zn} defects for CZTS1 (with Cu/Sn ~ 1.9) or with Cu_{Zn} defects for CZTS2 (with Cu/Sn ≥ 2.3). Otherwise, samples CZTS3 and CZTS4 belong to the more recently introduced kesterite types [6], which take into account that cationic disorder is also present for Zn/Sn ~ 1.0, producing Zn_{Cu} and Sn_{Cu} defects

under Cu-poor conditions or Cu_{Zn} and Cu_{Sn} for Cu-rich compositions. **The film thickness determined from cross-section SEM images (Figure S2) is t = 0.20 ± 0.02 µm, without significant change for the various samples with the heating temperature.**

The XRD patterns of all samples are shown in **Figure 1**, represented on a logarithmic scale for better identification of peaks with low intensity. These patterns evidence diffraction peaks at the main positions of the kesterite CZTS: (112), (220/204) and (116/312) planes, whatever the heating temperature. Other diffraction peaks corresponding to the kesterite planes (004/200), (301) and (224) are also found in some films. Only the CZTS2 sample shows a small additional peak of CuS, which remains virtually unchanged at 450 ºC or 500 ºC, while CZTS1 evidences a small peak of SnS after heating at 500 ºC. It should be noted that these secondary phases are in a lower proportion than observed for similar films [24,25], taking into account that here the diffraction intensity is on a logarithmic scale. Pure kesterite, without additional phases, has been obtained in the CZTS3 and CZTS4 layers.

The main diffraction peaks (**112, 220/204 and 116/312)** are normalized and overlaid plotted for the various samples in **Figure 2**. The change in the position and width of the peaks means a variation in the lattice volume and the crystallite size, which are represented as a function of the composition and the heating temperature in **Figure 3**. The mean crystallite size (S) is inversely proportional to the full width at half maximum of the diffraction peak (FWHM), according to the Scherrer formula [26], **taking into account the instrumental broadening**. The **lattice parameters (a, c)** and the cell volume ($V = a^2c$) have been obtained by measuring the interplanar spacings in the pattern, $d_{hkl} = \theta/(2\sin\theta)$, and applying the relation that corresponds to the tetragonal kesterite-type structure (with a = b): $1/(d_{hkl})^2 = (h^2+k^2)/a^2 + l^2/c^2$.

Figure 3 shows that the crystallite size (S) is in the range S_{112} = 28 - 53 nm for the samples annealed at 450 ºC, the lowest value corresponding to CZTS3 and the highest to CZTS4. The increment in the heating temperature to 500 ºC causes the mean crystallite size to grow to S_{112} = 40 - 53 nm, an increase of about 10 nm for the various layers except for CZTS4, which exhibits S_{112} = 53 nm regardless of the heating temperature. The **lattice parameters and the cell** volume in general disclose small variations with composition and temperature, being near to the standard value for kesterite CZTS powder (**c/a = 2.001** and V = 320 $Å^3$). An exception is found for the sample with the poorest crystallinity, CZTS3 heated at

450 ºC, which shows a higher volume of 326 $Å^3$ **corresponding to a lattice distortion c/a = 2.216**, but the volume decreases to 318 $Å^3$ **and the distortion to c/a = 2.000** when the crystallite size increases by heating at 500 ºC. In other CZTS thin films, the volume of the unit cell increases with the addition of Zn and decreases with the addition of Sn [6,26], but here the volume remains virtually the same irrespective of the different Zn/Sn ratios, being more dependent on the crystallite size. This is because a lower crystallite size is related to a higher lattice strain, as has been reported [11,22]. Increasing the temperature to 500 ºC causes greater mobility and surface diffusion, which favors the migration and coalesce of the deposited material, giving a larger crystallite size and a smaller lattice volume. Nevertheless, the CZTS4 sample exhibits the best crystallinity even at a lower temperature.

The morphology of the layers is illustrated by the SEM images in Figure 4. All the CZTS films have a dense microstructure with small grains and some agglomerations that are more evident for the samples with a higher Cu content (CZTS2 and CZTS4), such as it is commonly found for CZTS films prepared by different ways [27,28]. The diameter of the grains is generally greater than 100 nm, which indicates that the grains are constituted by several crystallites. As the annealing temperature increases, an enlargement of the grains is observed by SEM, in accordance with the increase in crystallite size (S) detected by X-ray diffraction. Increasing the grain size can improve the electrical conductivity of a polycrystalline CZTS thin film because the existence of less grain boundaries allows the effective diffusion length of carriers to increase.

Figure 5 shows the resistivity of the various samples, which varies in the interval $\rho = 10^{-2} – 10^{1}$ Ω cm. These values are within the range reported for other CZTS thin films [24,27,29]. The resistivity tends to decrease with increasing annealing temperature and Cu-rich samples (CZTS2 and CZTS4) have the lowest resistivity. This might be attributed to the crystalline improvement with the annealing temperature and the Cu-content, since a larger crystallite size results in fewer grain boundaries [24]. Furthermore, the resistivity is found practically unchanged while the Zn content increases from Zn/Sn = 0.5 (CZTS2) to Zn/Sn = 1.0 (CZTS4), in the same way that is observed in other works when Cu/(Zn+Sn) ≥ 1.0 [27]. In these kesterite materials, Cu vacancies could be responsible for the majority of hole carriers, but Cu_{Zn} antisites become the dominant acceptor whenever the growth conditions promote their formation [30], as it is the case for the present Cu-rich samples.

Light **absorptance** spectra (A) are plotted as a function of the photon energy (E) in Figure 6a. These spectra allow us to estimate the bandgap energy (E_g) as the inflection point of the **absorptance** curves [21], that is the peak of the derivative dA/dE, which is illustrated in **Figure 6b** for the various CZTS layers. When tailing is detected, a good approximation for the bandgap of extended states is the inflection point of the absorption curve in the low energy region [31,32]. Some absorption below the bandgap of extended states is usual in kesterites, as shown in Figure 6a. At low energies (below E_g) the **absorptance** is higher for Cu-rich layers (CZTS2 and CZTS4), but more similar values are obtained for all the samples at energies higher than E_g. The **absorptance** value taken at E = 2.25 eV, that is in the middle of the visible spectral range, is named visible **absorptance** (A_{vis}) and is represented in Figure 7 together with the respective E_g value (from Figure 6 b) for the different samples heated at 450 ºC and 500 ºC. The increase in temperature causes A_{vis} to decrease slightly, being always a minimum for CZTS3 (with A_{vis} ~ 70%) and a maximum for CZTS1 (A_{vis} ~ 85 %). Otherwise, the bandgap energy is found increasing from E_g = 0.95 eV for CZTS1 to E_g = 1.20 eV for CZTS4, with only small variations (± 0.02 eV) for the same sample heated at 450 ºC or 500 ºC.

It is known that various self-compensated defect clusters can grow in kesterite compounds, with overall formation energies significantly lower than the sum of isolated ones [33]. Figure 8 plots the schematic band structure for different defect clusters [3,33], corresponding to the off-stoichiometry of the various samples. For Cu_2ZnSnS_4, the maximum of the valence band (VB) is contributed by the Cu-3d and S-3p states and the minimum of the conduction band (CB) is derived from the Sn-5s and S-3p states [34]. In the perfect semiconductor the band edges (VB and CB) are separated by 1.50 eV (**Figure S3**), but the presence of defect clusters produces changes in the optical bandgap energy. The most significant changes are related to clusters composed of deep level defects, such as the Sn_{Zn} donor and V_{Zn} acceptor states [33]. On the other hand, Cu_{Zn} is not considered a deep acceptor state (although it is deeper than V_{Cu}), but the ($2Cu_{Zn}$ + Sn_{Zn}) cluster has a low formation energy and it is responsible for a significant reduction of the bandgap in CZTS [35]. The schematic diagram of Figure 8 explains the E_g value obtained for each layer according to the existing defects and their respective energy levels taken from the bibliography. This confirms the classification established in Table 2 for the different samples according to their atomic composition.

4. Conclusions

Kesterite thin films with controlled off-stoichiometry (types H, C, L and K) have been synthetized by sequential evaporation of chalcogenide precursors and subsequent sulfurization at 450 ºC or 500 ºC. K-type kesterite (with Zn/Sn ~ 1.0 and Cu/Sn ~ 3.0, obtained by reaction of Cu_3SnS_4 and ZnS) shows the best characteristics, with a high crystallite size of 53 nm, a low resistivity of 10^{-2} Ωcm and a wide gap of 1.20 eV, regardless of the heating temperature. The other three samples (with Zn/Sn ≤ 1.0 and Cu/Sn ≤ 2.5) have a crystallite size below 40 nm after heating at 450 ºC, increasing by 10 nm at 500 ºC. H-type kesterite (with Zn/Sn < 1.0 and Cu/Sn ~ 2.0) has the highest resistivity (above 40 Ω cm) and the lowest gap energy (~ 0.95 eV), which is related to the presence of deep Sn_{Zn} and V_{Zn} states. Intermediate bandgap values are obtained for C-type and L-type samples (1.0 eV and 1.1 eV, respectively), being the resistivity lower for Cu-rich layers due to the presence of Cu_{Zn} antisites that act as acceptors.

Acknowledgements

This research did not receive any specific grant from funding agencies. The postdoctoral stay carried out by the PhD. P. Martínez-Ortiz at CIEMAT was supported through the scholarship for postdoctoral stays abroad (Announcement 2019) by CONACYT.

We also appreciate the technical support provided by CIMAV, allowing access to the FESEM facilities of the National Nanotechnology Laboratory (NanoTech).

References

[1] K.S. Gour, V. Karade, P. Babar, J. Park, D.M. Lee, V.N. Singh, et al., Potential role of kesterites in development of earth-abundant elements-based next generation technology, Sol. RRL. 5 (2021) 2000815. doi:10.1002/solr.202000815.

[2] M. He, C. Yan, J. Li, M.P. Suryawanshi, J. Kim, M.A. Green, et al., Kesterite solar cells: insights into current strategies and challenges, Adv. Sci. 8 (2021) 2004313. doi:10.1002/advs.202004313.

[3] S. Chen, A. Walsh, X.G. Gong, S.H. Wei, Classification of lattice defects in the kesterite Cu_2ZnSnS_4 and $Cu_2ZnSnSe_4$ earth-abundant solar cell absorbers, Adv. Mater. 25 (2013) 1522–1539. doi:10.1002/adma.201203146.

[4] K. Rudisch, A. Davydova, C. Platzer-Björkman, J. Scragg, The effect of stoichiometry on Cu-Zn ordering kinetics in Cu_2ZnSnS_4 thin films, J. Appl. Phys. 123 (2018) 161558. doi:10.1063/1.5010081.

[5] L.E. Valle Rios, K. Neldner, G. Gurieva, S. Schorr, Existence of off-stoichiometric single phase kesterite, J. Alloys Compd. 657 (2016) 408–413. doi:10.1016/j.jallcom.2015.09.198.

[6] G. Gurieva, L.E. Valle Rios, A. Franz, P. Whitfield, S. Schorr, Intrinsic point defects in off-stoichiometric $Cu_2ZnSnSe_4$: A neutron diffraction study, J. Appl. Phys. 123 (2018) 161519. doi:10.1063/1.4997402.

[7] G. Gurieva, R. Ferreira, P. Knoll, S. Schorr, $Cu_2ZnSnSe_4$: How far does off-stoichiometry go?, Phys. Status Solidi. 215 (2018) 1700957. doi:10.1002/pssa.201700957.

[8] S. Schorr, G. Gurieva, M. Guc, M. Dimitrievska, A. Pérez-Rodríguez, V. Izquierdo-Roca, et al., Point defects, compositional fluctuations, and secondary phases in non-stoichiometric kesterites, J. Phys. Energy. 2 (2019) 12002. doi:10.1088/2515-7655/ab4a25.

[9] M. Lang, T. Renz, N. Mathes, M. Neuwirth, T. Schnabel, H. Kalt, et al., Influence of the Cu content in $Cu_2ZnSn(S,Se)_4$ solar cell absorbers on order-disorder related band gap changes, Appl. Phys. Lett. 109 (2016) 142103. doi:10.1063/1.4964346.

[10] J.K. Larsen, J.J.S. Scragg, N. Ross, C. Platzer-Björkman, Band tails and Cu–Zn disorder in Cu_2ZnSnS_4 solar cells, ACS Appl. Energy Mater. 3 (2020) 7520–7526. doi:10.1021/acsaem.0c00926.

[11] N.J. Choudhari, Y. Raviprakash, F. Bellarmine, M.S. Ramachandra Rao, R. Pinto, Investigation on the sulfurization temperature dependent phase and defect formation of sequentially evaporated Cu-rich CZTS thin films, Sol. Energy. 201 (2020) 348–361. doi:10.1016/j.solener.2020.03.007.

[12] S. Exarhos, E. Palmes, L. Mangolini, Structural homogenization and cation ordering in CZTS films during sulfurization as probed via in-situ Raman, Thin Solid Films. 684 (2019) 21–30. doi:10.1016/j.tsf.2019.05.048.

[13] C. Sripan, V.E. Madhavan, A.K. Viswanath, R. Ganesan, Sulfurization and annealing effects on thermally evaporated CZTS films, Mater. Lett. 189 (2017) 110–113. doi:10.1016/j.matlet.2016.11.094.

[14] V. Robles, C. Guillén, J.F. Trigo, J. Herrero, Cu_2ZnSnS_4 thin films obtained by sulfurization of evaporated Cu_2SnS_3 and ZnS layers: Influence of the ternary precursor features, Appl. Surf. Sci. 400 (2017). doi:10.1016/j.apsusc.2016.12.186.

[15] A. Weber, R. Mainz, H.W. Schock, On the Sn loss from thin films of the material system Cu–Zn–Sn–S in high vacuum, J. Appl. Phys. 107 (2010) 13516.

doi:10.1063/1.3273495.

[16] E.A. Lund, H. Du, W.M. Hlaing Oo, G. Teeter, M.A. Scarpulla, Investigation of combinatorial coevaporated thin film Cu_2ZnSnS_4 (II): Beneficial cation arrangement in Cu-rich growth, J. Appl. Phys. 115 (2014) 173503. doi:10.1063/1.4871665.

[17] V. Robles, J.F. Trigo, C. Guillén, J. Herrero, Copper tin sulfide (CTS) absorber thin films obtained by co-evaporation: Influence of the ratio Cu/Sn, J. Alloys Compd. 642 (2015) 40–44. doi:10.1016/j.jallcom.2015.04.104.

[18] V. Robles, J.F. Trigo, C. Guillén, J. Herrero, Copper tin sulfide (CuxSnSy) thin films evaporated with x=3,4 atomic ratios: influence of the substrate temperature and the subsequent annealing in sulfur, Mater. Res. Bull. 83 (2016) 116–121. doi:10.1016/j.materresbull.2016.05.015.

[19] C.A. Macías-Cabrera, J. Campos-Álvarez, S.A. Gamboa, J.A. Aguilar-Martínez, Y. Peña-Méndez, Synthesis of CZTS thin films from binary precursors stacking by chemical bath deposition for solar cell applications, Mater. Today Proc. 46 (2021) 3109–3113. doi:10.1016/j.matpr.2021.02.624.

[20] P. Bais, M.T. Caldes, C. Guillot-Deudon, A. Renaud, M. Boujtita, S. Jobic, et al., Influence of the copper deficiency and anionic composition on band-energy diagram of bulk kesterite CZTSSe, Mater. Res. Bull. 139 (2021). doi:10.1016/j.materresbull.2021.111285.

[21] J.A. Márquez, M. Rusu, H. Hempel, I.Y. Ahmet, M. Kölbach, I. Simsek, et al., $BaZrS_3$ chalcogenide perovskite thin films by H_2S sulfurization of oxide precursors, J. Phys. Chem. Lett. 12 (2021) 2148–2153. doi:10.1021/acs.jpclett.1c00177.

[22] A. Sharmin, M.S. Bashar, M. Sultana, S.M.M. Al Mamun, Sputtered single-phase kesterite Cu_2ZnSnS_4 (CZTS) thin film for photovoltaic applications: Post annealing parameter optimization and property analysis, AIP Adv. 10 (2020). doi:10.1063/1.5129202.

[23] H.R. Jung, S.W. Shin, K. V. Gurav, M.G. Gang, J.Y. Lee, J.H. Moon, et al., Evolution of detrimental secondary phases in unstable Cu_2ZnSnS_4 films during annealing, Electron. Mater. Lett. 12 (2016) 139–146. doi:10.1007/s13391-015-5340-2.

[24] M.A. Olgar, A. Seyhan, A.O. Sarp, R. Zan, The choice of Zn or ZnS layer in the stacked precursors for preparation of Cu_2ZnSnS_4 (CZTS) thin films, Superlattices Microstruct. 146 (2020) 106669. doi:10.1016/j.spmi.2020.106669.

[25] T.G. Sánchez, X. Mathew, N.R. Mathews, Obtaining phase-pure CZTS thin films by annealing vacuum evaporated CuS/SnS/ZnS stack, J. Cryst. Growth. 445 (2016) 15–23.

doi:10.1016/j.jcrysgro.2016.03.039.

[26] T. Chandel, M.B. Zaman, S.K. Dwivedi, R. Poolla, Structural, morphological and optical properties of sprayed Cu_2ZnSnS_4 thin films by varying the molar concentration of Zn & Sn, Vacuum. 159 (2019) 341–345. doi:10.1016/j.vacuum.2018.10.032.

[27] T. Tanaka, A. Yoshida, D. Saiki, K. Saito, Q. Guo, M. Nishio, et al., Influence of composition ratio on properties of Cu_2ZnSnS_4 thin films fabricated by co-evaporation, Thin Solid Films. 518 (2010) S29–S33. doi:10.1016/j.tsf.2010.03.026.

[28] S.M. Bhosale, M.P. Suryawanshi, J.H. Kim, A.V. Moholkar, Influence of copper concentration on sprayed CZTS thin films deposited at high temperature, Ceram. Int. 41 (2015) 8299–8304. doi:10.1016/j.ceramint.2015.02.124.

[29] P. Prabeesh, I. Packia Selvam, S.N. Potty, CZTS films from three different routes: Crystallite size-dependent properties, Mater. Res. Express. 6 (2019). doi:10.1088/2053-1591/ab08d5.

[30] D. Han, Y.Y. Sun, J. Bang, Y.Y. Zhang, H.B. Sun, X. Bin Li, et al., Deep electron traps and origin of p-type conductivity in the earth-abundant solar-cell material Cu_2ZnSnS_4, Phys. Rev. B - Condens. Matter Mater. Phys. 87 (2013) 1–5. doi:10.1103/PhysRevB.87.155206.

[31] W. Wang, M.T. Winkler, O. Gunawan, T. Gokmen, T.K. Todorov, Y. Zhu, et al., Device characteristics of CZTSSe thin-film solar cells with 12.6% efficiency, Adv. Energy Mater. 4 (2014) 1301465. doi:10.1002/aenm.201301465.

[32] S. Siebentritt, G. Rey, A. Finger, D. Regesch, J. Sendler, T.P. Weiss, et al., What is the bandgap of kesterite?, Sol. Energy Mater. Sol. Cells. 158 (2016) 126–129. doi:10.1016/j.solmat.2015.10.017.

[33] S. Chen, J.H. Yang, X.G. Gong, A. Walsh, S.H. Wei, Intrinsic point defects and complexes in the quaternary kesterite semiconductor Cu_2ZnSnS_4, Phys. Rev. B - Condens. Matter Mater. Phys. 81 (2010) 245204. doi:10.1103/PhysRevB.81.245204.

[34] D. Liu, D. Han, M. Huang, X. Zhang, T. Zhang, C. Dai, et al., Theoretical study on the kesterite solar cells based on $Cu_2ZnSn(S,Se)_4$ and related photovoltaic semiconductors, Chinese Phys. B. 27 (2018) 18806. doi:10.1088/1674-1056/27/1/018806.

[35] A. Crovetto, S. Kim, M. Fischer, N. Stenger, A. Walsh, I. Chorkendorff, et al., Assessing the defect tolerance of kesterite-inspired solar absorbers, Energy Environ. Sci. 13 (2020) 3489–3503. doi:10.1039/d0ee02177f.

Table 1. Precursors chosen for the various CZTS thin films.

Sample name	Precursor sequence	Targeted composition
CZTS1	$Cu_2SnS_3 + 0.5ZnS$	$Cu_{2.0}Zn_{0.5}SnS_{3.5}$
CZTS2	$Cu_{2.3}SnS_3 + 0.5ZnS$	$Cu_{2.3}Zn_{0.5}SnS_{3.5}$
CZTS3	$Cu_2SnS_3 + ZnS$	$Cu_{2.0}Zn_{1.0}SnS_4$
CZTS4	$Cu_3SnS_4 + ZnS$	$Cu_{3.0}Zn_{1.0}SnS_4$

Table 2. Composition data obtained by EDX for the various CZTS samples heated at 450 ºC or 500 ºC. The off-stoichiometry kesterite type and the corresponding defects cluster are assigned according to the literature [6,8].

Sample	T (ºC)	Cu:Zn:Sn:S (%at)	EDX composition	Kesterite type and related defects [6,8]
CZTS1	450	33:10:18:39	$Cu_{1.8}Zn_{0.6}SnS_{2.2}$	H-type: $Sn_{Zn} + V_{Zn}$
	500	33:11:17:39	$Cu_{1.9}Zn_{0.6}SnS_{2.3}$	
CZTS2	450	37:8:16:39	$Cu_{2.3}Zn_{0.5}SnS_{2.4}$	C-type: $Sn_{Zn} + 2Cu_{Zn}$
	500	37:9:15:39	$Cu_{2.5}Zn_{0.6}SnS_{2.6}$	
CZTS3	450	34:14:16:36	$Cu_{2.1}Zn_{0.9}SnS_{2.3}$	L-type: $Zn_{Cu} + Sn_{Cu} + V_{Cu}$
	500	34:15:15:36	$Cu_{2.2}Zn_{1.0}SnS_{2.4}$	
CZTS4	450	37:13:12:38	$Cu_{3.1}Zn_{1.1}SnS_{3.2}$	K-type: $Cu_{Zn} + Cu_{Sn} + 4Cu_i$
	500	37:12:13:38	$Cu_{2.8}Zn_{0.9}SnS_{2.9}$	

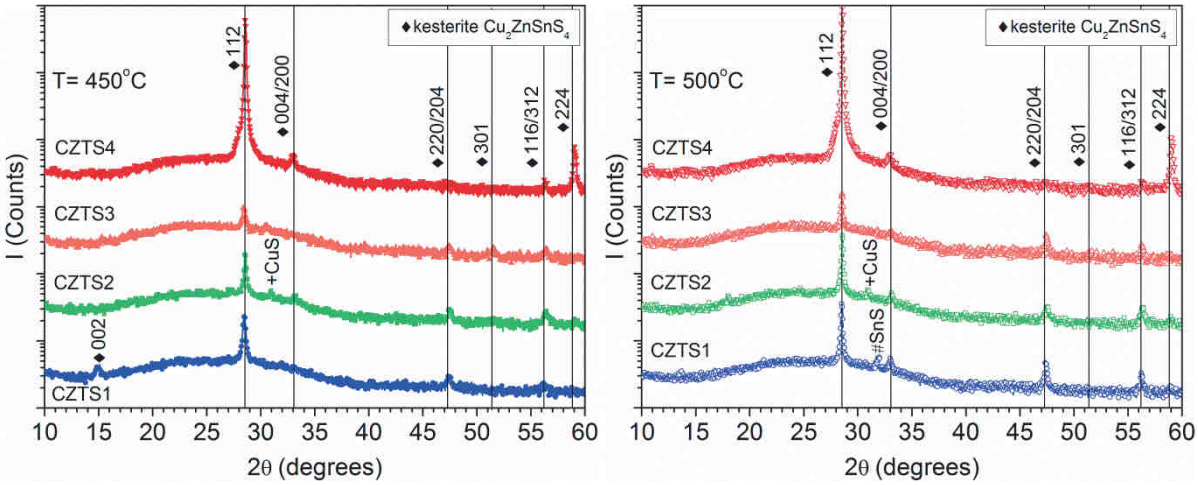

Figure 1. XRD patterns for the various CZTS samples heated at 450 ºC or 500 ºC. Peaks are indexed according to the standard file for kesterite Cu_2ZnSnS_4 (**PDF#04-015-0223**).

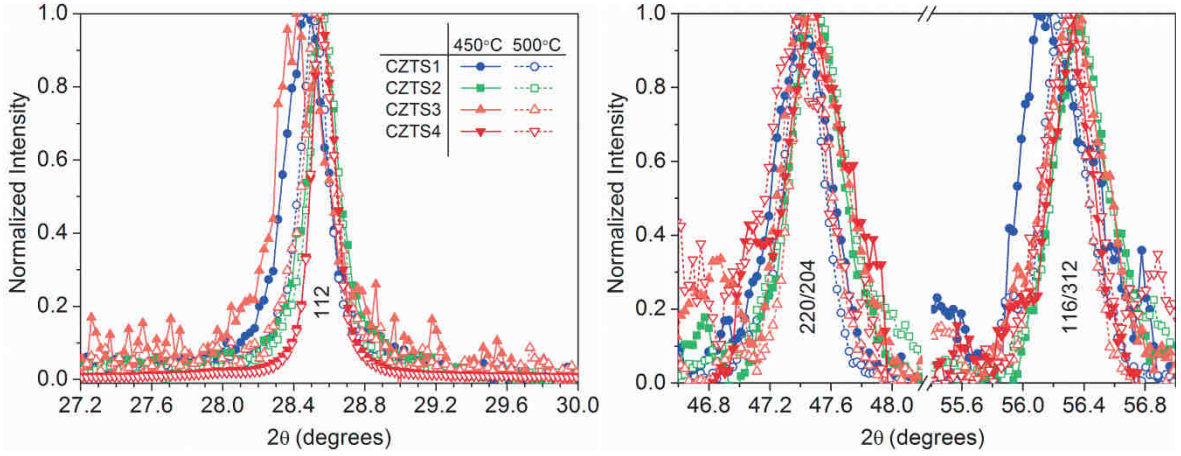

Figure 2. Comparison of the main diffraction peaks **(112, 220/204 and 116/312)** for the same CZTS samples represented in Figure 1.

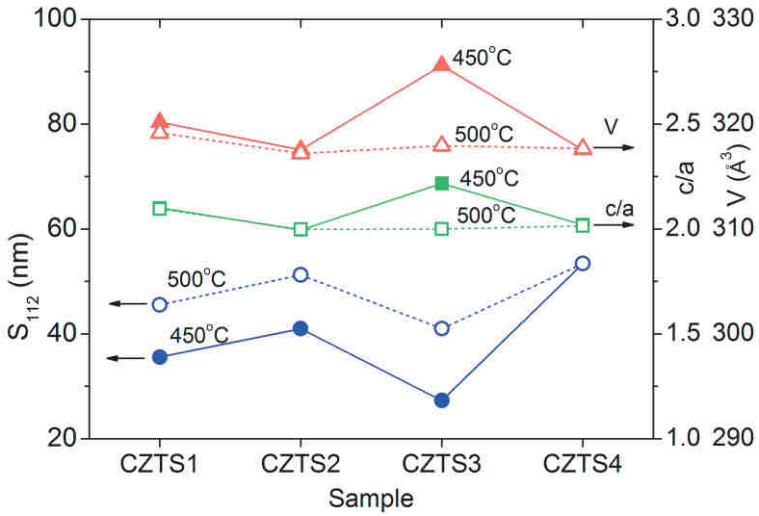

Figure 3. Mean crystallite size (S_{112}), **lattice parameter ratio (c/a)** and crystalline cell volume (V) for the CZTS samples heated at 450 ºC or 500 ºC.

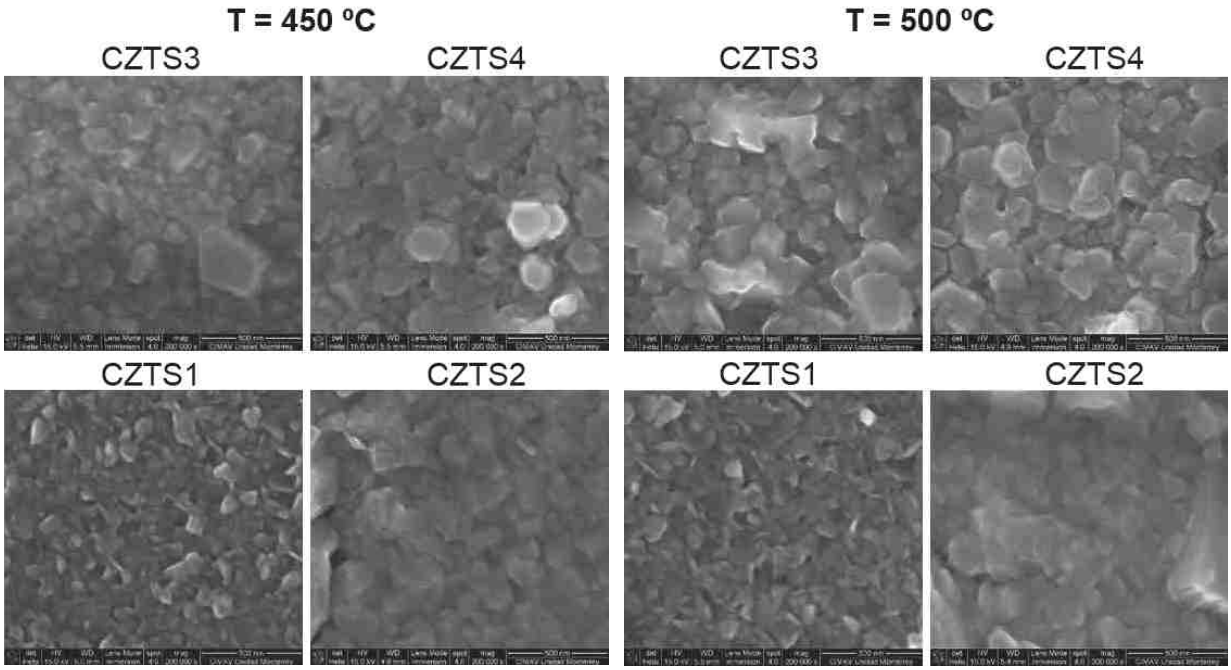

Figure 4. SEM images (magnification x200k) for the various CZTS samples.

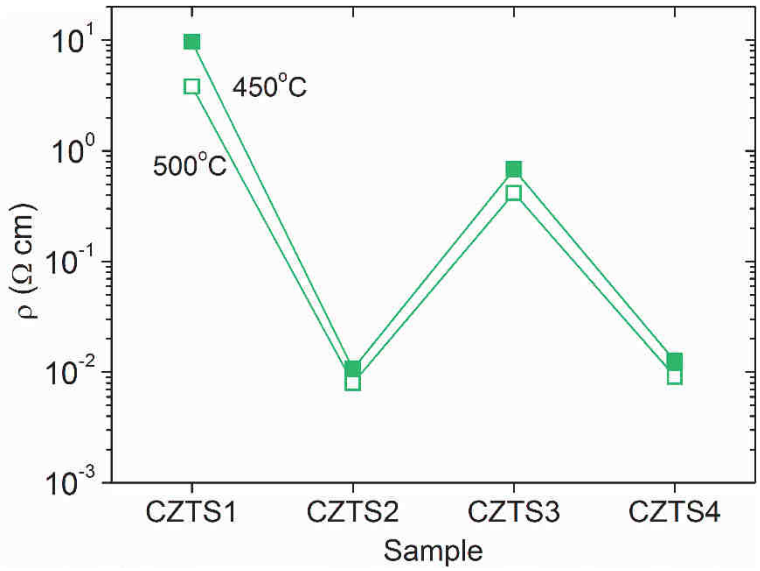

Figure 5. Electrical resistivity for the CZTS samples heated at 450 ºC or 500 ºC.

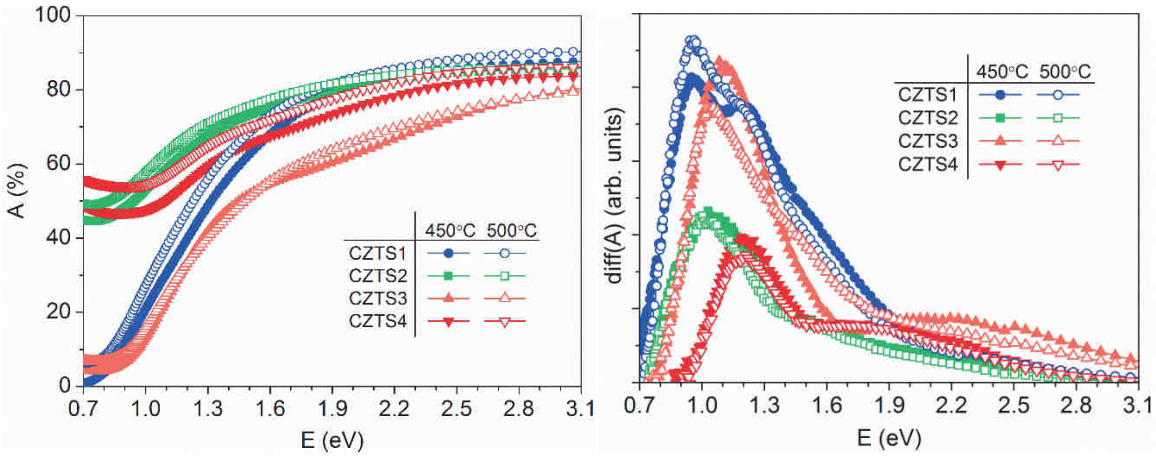

Figure 6. Optical characteristics of the different CZTS samples: a) **absorptance** curves as a function of the photon energy (A vs. E), b) differential of the **absorptance** curves (from the derivative dA/dE).

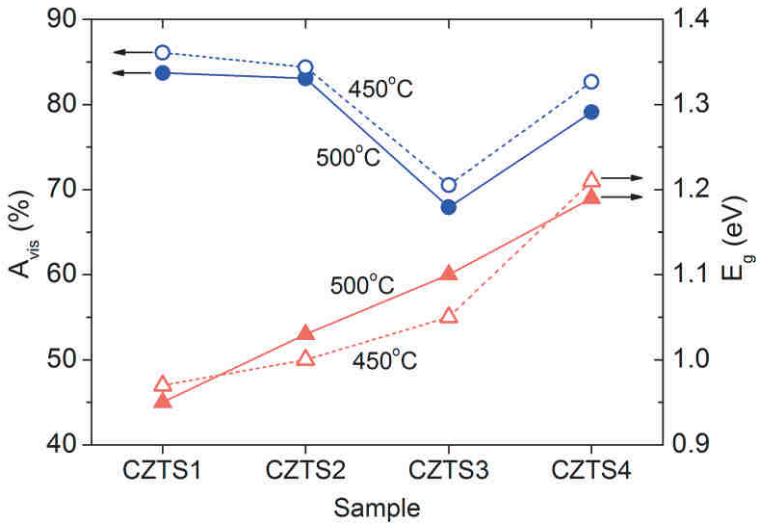

Figure 7. Visible **absorptance** (A_{vis}) and bandgap energy (E_g) for the CZTS samples heated at 450 ºC or 500 ºC.

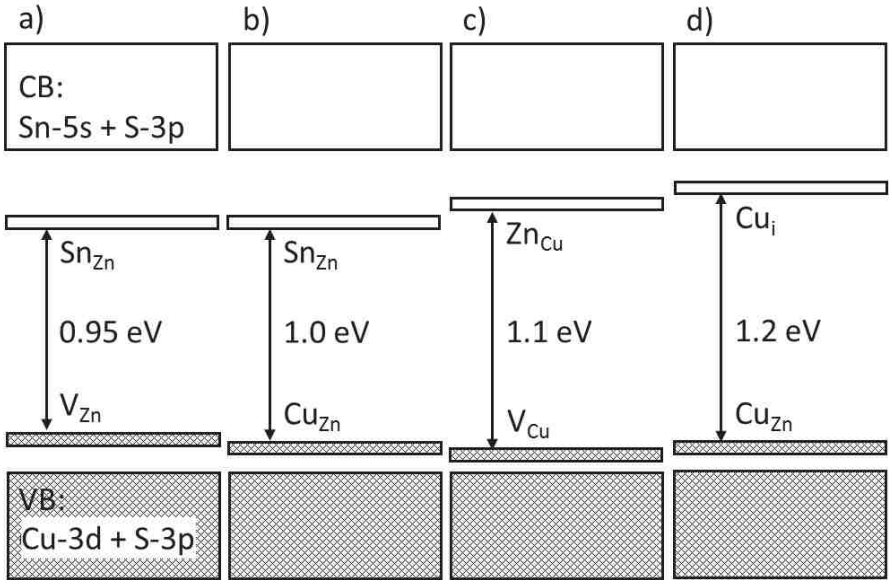

Figure 8. Schematic diagram showing optical transition energy for the various kesterite samples, depending on the main defects [3]: a) CZTS1 with Sn_{Zn} and V_{Zn} defects, b) CZTS2 with Sn_{Zn} and Cu_{Zn} defects, c) CZTS3 with Zn_{Cu} and V_{Cu} defects and d) CZTS4 with Cu_i and Cu_{Zn} defects. The filled states in each case correspond to the shaded areas.